FDMP, vol.4, no.1, pp.27-41, 2008

A Deterministic Mechanism for Side-branching in Dendritic Growth

Shuwang Li[1], Xiangrong Li[1], John Lowengrub[1,2] and Martin Glicksman[3]

Abstract: In this paper, we suggest a deterministic mechanism for the generation and development of side-branches in dendritic growth. The present authors investigated recently [Glicksman, Lowengrub, and Li (2006)] the existence of such a deterministic branching mechanism induced through the Gibbs-Thomson-Herring (GTH [Herring (1951)]) anisotropic capillary boundary condition. In this paper, we focus our study on an anisotropic kinetic boundary condition. We develop and apply accurate boundary integral methods in 2D and 3D, in which a time and space rescaling scheme is implemented, that are capable of separating the dynamics of growth from those of morphology change. Numerical results reveal that under anisotropic kinetic boundary conditions a non-monotone temperature distribution forms on the interface near the tip that leads to oscillations of the scaled tip velocity. This dynamical process resembles a limit cycle that generates a sequence of time-periodic protuberances near the tip. These protuberances propagate away from the tip and develop into side-branches at later times. Unlike the conventional noise-amplification theory [Pieters and Langer (1986)], the generation and development of side-branches is intrinsic, and occurs solely under the deterministic influence of the anisotropic kinetic boundary condition.

Keyword: dendrites, side-branching, solidification, boundary integral.

1 Introduction

Dendrites growing from supercooled melts or supersaturated solutions are characterized by smooth, parabolic-like tips with side-branches behind them. Understanding the formation of dendritic structures has long been a challenging research topic in materials science. Through a combination of analysis, numerics and experiments [e.g. LaCombe, Koss, Frei, Giummarra, Lupulescu, and Glicksman (2002); Giummarra, LaCombe, Koss, Frei, Lupulescu, and Glicksman (2005); Pieters and Langer (1986); Jacob and Garik (1990); McFadden, Coriell, and Sekerka (2000a,b); Kim, Goldenfeld, and Dantzig (2000); Jeong, Goldenfeld, and Dantzig (2001); Glicksman, Schaefer, and Ayers (1976); Nash and Glicksman (1974a,b); Ihle (2000); Dougherty, Kaplan, and Gollub (1987); Karma and Rappel (1999); Almgren, Dai, and Hakim (1993); Martin and Goldenfeld (1987); Couder, Cardoso, Dupuy, Tavernier, and Thom (1986); Couder, Gerard, and Rabaud (1986); Hong, Zhu, and Lee (2006); Narski and Picasso (2007); Borzsonyi, Toth-Katona, Buka, and Granasy (2000)], it is now recognized that anisotropies in surface tension and/or in the atomic attachment kinetics play an important role to stabilize the advancing dendritic tip region against splitting. The physical mechanism that determines the generation and development of side-branches, however, remains a subject of controversy.

The conventional theory for the formation of side-branches, first proposed by Pieters and Langer [Pieters and Langer (1986)], postulates that dendritic side-branches may be generated by selective noise amplification near the tip, and, moreover, the sources of noise are thermal fluctuations in the system. Using a two dimensional boundary-layer model with kinetic crystalline anisotropy, their

---

[1] Department of Mathematics, University of California at Irvine, Irvine CA 92697

[2] Corresponding author. Department of Chemical Engineering and Material Science, University of California at Irvine, Irvine CA 92697

[3] Department of Material Science and Engineering, University of Florida, Gainesville, FL 32611

numerical results and linear asymptotic analysis suggest that a small random perturbation added to the tip velocity can be amplified to form visible side-branches. Measurements of the dendritic growth of NH_4Br crystals from supersaturated solution by Dougherty appear consistent with the conventional noise amplification proposition in that the observed side-branches on opposite sides of the dendrite are imperfectly correlated with variations appearing in both phase and amplitude [Dougherty, Kaplan, and Gollub (1987)]. These observations agree with the stochastic nature of noise amplification theory, although the precise origin of noise in Dougherty's experiment is unknown.

Martin and Goldenfeld, using a geometrical model, investigated the existence of a deterministic mechanism for the formation of side-branches within the framework of an eigenmode analysis of a linear stability operator [Martin and Goldenfeld (1987)]. They presented several possible reasons for the generation of side-branches in dendritic growth, such as a limit cycle behavior due to a Hopf bifurcation and a solvability-induced side-branching [Martin and Goldenfeld (1987)]. Their analysis emphasizes the importance of nonlinear effects and suggests that the combination of both nonlinear dynamics and the singular nature of the steady state is responsible for side-branching [Martin and Goldenfeld (1987)]. Experimental results [Couder, Cardoso, Dupuy, Tavernier, and Thom (1986); Couder, Gerard, and Rabaud (1986)] show that nonlinear effects play an important role in the generation of side-branches. In these experiments, a small air bubble is placed at the tip of a viscous finger developing in a Hele-Shaw cell. The nonlinear interaction between the small air bubble and the finger tip gives rise to the generation of well-correlated side-branches on either side of the finger. These observations suggest that noise is not important here. Similar phenomena were also observed in liquid crystals. Borzsonyi, Toth-Katona, Buka, and Granasy (2000) demonstrated that by applying a nonlocal periodic force (e.g. time-periodic pressure or heating) in the vicinity of a liquid crystal dendrite tip, the resulting tip velocity became oscillatory and side-branches were regularized by these forces, i.e., the side-branches became nearly periodic, again indicating that noise amplification was not important here either. Using non-Newtonian fluids, Kondic, Palffy-Muhoray, Shelley and Fast [Kondic, Palffy-Muhoray, and Shelley (1996, 1997); Fast, Kondic, Palffy-Muhoray, and Shelley (2001)] found that a shear-rate dependent viscosity of the driven fluid significantly influences pattern formation in a Hele-Shaw cell. In particular, shear thinning suppresses tip-splitting and produces fingers that grow in an oscillatory manner, periodically developing side-branches behind their tips. These results strongly suggest that an oscillatory tip velocity might be important to the generation and development of dendritic side-branches, which although recognized previously in Pieters and Langer's work [Pieters and Langer (1986)] was ascribed to a non-deterministic origin.

Noise amplification theory certainly seems to provide an explanation of side-branching in some dendritic systems, but the experimental and theoretical results mentioned above suggest that deterministic mechanisms may also exist for side-branching that warrant further examination. The existence of such a mechanism for the Gibbs-Thomson-Herring (GTH) anisotropic capillary boundary condition was investigated recently by the present authors [Glicksman, Lowengrub, and Li (2006)]. In this paper, we focus our study on an evolving crystal subject to an anisotropic kinetic boundary condition. We develop accurate 2D and 3D boundary integral methods in which a time and space rescaling scheme is implemented in a manner such that the area/volume of the crystal appears unchanged. Specifically, we exposed the detailed dynamics of the evolving dendrite tip subject to anisotropic interface kinetics by scaling out the overall growth of the crystal. Our numerical results reveal that the interface can develop periodic non-monotone temperature distributions that lead to oscillations of the scaled tip velocity. This dynamical process acts like a limit cycle and generates a time-periodic sequence of protuberances near the tip that propagate away from the tip and form side-branches at later times. Unlike conventional noise-amplification theory [Pieters and Langer (1986)], the formation of side-branches is intrinsic and occurs solely under the influence of the anisotropic kinetic boundary condition without any significant noise present.

This paper is organized as follows: in section 2, we review the governing equations; in section 3, we present the rescaling scheme; in section 4, we discuss the numerical results; and in section 5, we provide conclusions.

2 Governing Equations

In this paper, we consider a crystal growing quasi-statically in a supercooled pure melt. The interface Σ separates the solid phase Ω_1 from the melt Ω_2. We assume for simplicity that the surface tension γ along the interface is isotropic, and the interfacial kinetic coefficient is 4-fold anisotropic, *i.e.* $\varepsilon(\mathbf{n}) = \varepsilon_0(1-\beta\left(3-4\left(n_1^4+n_2^4+n_3^4\right)\right))$ where n_i denotes the components of the normal vector $\mathbf{n}$. In 2D, this anisotropic form reduces to $\varepsilon(\theta) = \varepsilon_0(1+\mu\cos(4\theta))$, where θ is the angle between the normal vector and a fixed axis, and μ represents the strength of the kinetic anisotropy. For simplicity, the thermal diffusivities of the two phases are assumed to be identical. The length scale is the equivalent radius of the crystal (R_0, radius of a sphere/circle with the same volume/area) at time $t = 0$, where the time scale is the characteristic surface tension relaxation time scale [Li, Lowengrub, Leo, and Cristini (2004, 2005); Li, Lowengrub, and Leo (2005)]. The temperature is non-dimensionalized by $\dfrac{Temp-T_{ph}}{\Delta T_\gamma}$, where $Temp$ is the dimensional temperature in Ω_1 and Ω_2; T_{ph} is the phase change temperature for a flat interface; $\Delta T_\gamma = \gamma T_{ph}/(\mathscr{L}R_0)$, where $\mathscr{L}$ is the latent heat per unit volume and isotropic surface tension $\gamma = 1$. The following non-dimensional equations govern the growth of the crystal:

$$\nabla^2 T_i = 0 \qquad \text{in } \Omega_i \quad \text{i=1, 2}, \tag{1}$$

$$V = (\nabla T_1 - \nabla T_2)\cdot\mathbf{n} \quad \text{on } \Sigma, \tag{2}$$

$$T_1 = T_2 = -\kappa - \varepsilon(\mathbf{n})V \quad \text{on } \Sigma, \tag{3}$$

$$J = \frac{1}{2(N-1)\pi}\int_\Sigma V d\Sigma, \tag{4}$$

where T_i is the temperature field, $i = 1$ for the solid phase and $i = 2$ for the melt, κ is the mean curvature, and J is the integral far-field heat flux and specifies the time derivative of the volume/area of the solid phase. $N = 2,3$ is the spatial dimension. In this paper, $J = C\cdot R(t)^{N-2}$ where R is the equivalent radius at time t, and C is a constant. This corresponds roughly to assuming a constant temperature condition at the far-field. The interface Σ evolves via

$$\mathbf{n}\cdot\frac{d\mathbf{x}}{dt} = V \qquad \text{on } \Sigma, \tag{5}$$

where V is the normal velocity of the interface and $\mathbf{n}$ is the unit normal directed towards Ω_2.

Equation (3) implements the standard anisotropic kinetic boundary condition. The kinetic coefficient reflects the underlying crystallographic orientation (4-fold cubic symmetry) and represents the free energy 'cost' for a finite rate of molecular attachment from the melt to the crystalline phase. A non-zero, anisotropic interfacial kinetic coefficient causes the moving interface to depart from its local equilibrium temperature, consume free energy, and follow preferred growth directions.

Since the temperature fields in both solid and liquid phases are harmonic, the temperature may be given as a single-layer potential. This yields Fredholm integral equations of the second-kind [Mikhlin (1957)] for $V(\mathbf{x})$ and $T_\infty(t)$, where the latter is the far-field temperature. This procedure yields,

$$-\kappa(\mathbf{x}) - \varepsilon(\mathbf{n})V = \int_\Sigma G(\mathbf{x}-\mathbf{x}')V(\mathbf{X}')d\Sigma(\mathbf{x}') + T_\infty, \tag{6}$$

and

$$J = \frac{1}{2(N-1)\pi}\int_\Sigma V(\mathbf{x}')d\Sigma(\mathbf{x}'), \tag{7}$$

where $G(\mathbf{x}) = \frac{1}{2\pi}\log|\mathbf{x}|$ in 2D and $G(\mathbf{x}) = \frac{1}{4\pi}1/|\mathbf{x}|$ in 3D are the appropriate Green's functions.

3 Time and space rescaling scheme

In order to simulate accurately and efficiently the nonlinear dynamics of the evolving crystal, we use 2D and 3D boundary integral methods in which a time and space rescaling is implemented. The methods are capable of separating the dynamics of growth from those of morphology change. This separation exposes more clearly the processes underlying side-branching. We successfully implemented this scheme to study the long-time dynamics of a growing crystal [Cristini and Lowengrub (2004); Li, Lowengrub, Leo, and Cristini (2005); Li, Lowengrub, and Leo (2005)] and viscous fingering in a Hele-Shaw cell [Li, Lowengrub, and Leo (2007)]. The method is described briefly below.

We introduce the following spatial and temporal scaling

$$\mathbf{x} = \overline{R}(\bar{t})\bar{\mathbf{x}}(\bar{t},\alpha), \tag{8}$$

and

$$\bar{t} = \int_0^t \frac{1}{\rho(t')}dt', \tag{9}$$

where $\overline{R}(\bar{t}) = R(t(\bar{t}))$, and where $\bar{\mathbf{x}}(\bar{t},\alpha)$ is the position vector of the scaled interface, $\bar{t}$ represents the new time variable and ρ defines the new time scale. The scaling $\overline{R}$ is chosen such that the volume $\overline{Vol}$ in 3D and area $\overline{A}$ in 2D enclosed by the scaled interface is constant in time. The scaling $\overline{R}$ can be found by integrating the normal velocity over the interface to get

$$\frac{d\overline{R}(\bar{t})}{d\bar{t}} = \frac{\overline{\rho}(\bar{t})}{\overline{R}(\bar{t})^{N-1}\cdot\overline{Vol}}\cdot\frac{2(N-1)\pi}{N}\cdot\overline{J}(\bar{t}), \tag{10}$$

where $\overline{\rho}(\bar{t}) = \rho(t(\bar{t}))$ and analogously $\overline{J}(\bar{t}) = J(t(\bar{t}))$. We choose $\overline{\rho} = \frac{\overline{R}^N\overline{Vol}N}{2(N-1)\pi\overline{J}}$ following Eq. (10) to achieve exponential growth of $\overline{R}$ in the scaled frame.

The normal velocity in the new frame is $\overline{V}(\bar{t},\alpha) = \frac{d\bar{\mathbf{x}}(\bar{t},\alpha)}{d\bar{t}}\cdot\mathbf{n}$ and satisfies

$$-\overline{\kappa}\frac{\overline{\rho}}{\overline{R}^3} - \frac{\varepsilon(\mathbf{n})}{\overline{R}}\bar{\mathbf{x}}\cdot\mathbf{n} - \mathscr{G}[\bar{x}] = \int_{\Sigma} G(|\bar{\mathbf{x}}-\bar{\mathbf{x}}'|)\overline{V}ds' + \frac{\varepsilon(\mathbf{n})}{\overline{R}}\overline{V} + \overline{T}_\infty(\bar{t}), \tag{11}$$

and

$$0 = \int_{\Sigma}\overline{V}ds, \tag{12}$$

where $\overline{\kappa} = \overline{R}\kappa$ and the scaling factor $\overline{R}$ is

$$\overline{R}(\bar{t}) = \exp(\bar{t}). \tag{13}$$

Further, in Eq. (11) we have taken $\overline{T}_\infty(\bar{t}) = \frac{\overline{Vol}\log(\overline{R})}{\pi} + \frac{\overline{\rho}}{\overline{R}^2}T_\infty(t(\bar{t}))$ in 2D and $\overline{T}_\infty(\bar{t}) = \overline{\rho}T^\infty/\overline{R}^2$ in 3D, and $\mathscr{G}(\bar{\mathbf{x}}) = \int_{\Sigma}\bar{\mathbf{x}}'\cdot\mathbf{n}(\bar{\mathbf{x}}')G(\bar{\mathbf{x}}-\bar{\mathbf{x}}')ds'$.

To evolve the interface numerically, Eqs. (11) and (12) are discretized in space and solved efficiently using GMRES [Saad and Schultz (1986)]. In 2D, Eqs. (11) and (12) are discretized in space using spectrally accurate discretizations [Hou, Lowengrub, and Shelley (1994); Almgren, Dai, and Hakim (1993)]. The resulting discrete system is solved efficiently using a diagonal preconditioner in Fourier space [Hou, Lowengrub, and Shelley (1994); Jou, Leo, and Lowengrub (1997)].

In 3D, the surface is discretized using an adaptive surface triangulated mesh [Cristini, Blawzdziewicz, and Loewenberg (2001)]. The surface is then divided into three regions [Li, Cristini, Nie, and Lowengrub (2007)]: (1) a singular region that contains all the triangles with the evaluation point **x** as a vertex; (2) a quasi-singular region that is the collection of triangles the center of which is a distance d from **x**; and (3) a non-singular region that contains all other triangles. In the non-singular region, the Trapezoid rule is used to perform the integration. In the quasi-singular region, a seven-point Gaussian quadrature is used. In the singular region, Duffy's transformation is used to map the triangle to a unit square which removes the $1/r$ singularity and a seven-point Gaussian quadrature is then used. The discretized equations are solved using GMRES with a diagonal preconditioner. The curvature is approximated using a least-squares parabolic fit of the surface [Zinchenko, Rother, and Davis (1997)]. We note that the efficacy of using adaptive mesh (grid) algorithms to resolve moving interfaces have been well validated, see [Cristini, Blawzdziewicz, and

Loewenberg (2001); Sussman and Ohta (2007); Gibou, Min, and Ceniceros (2007)] for example.

Once $\overline{V}$ is obtained, the interface is evolved by using a second-order accurate non-stiff updating scheme in time and the equal arclength parameterization [Almgren, Dai, and Hakim (1993); Hou, Lowengrub, and Shelley (1994); Jou, Leo, and Lowengrub (1997)] in 2D and an explicit second-order Runge-Kutta method in 3D [Cristini and Lowengrub (2004); Li, Cristini, Nie, and Lowengrub (2007)].

4 Results

In order to isolate the effects of anisotropic kinetics on the formation of dendrite primary arms and side-branches, the initial crystal shape was chosen to be a unit circle or sphere.

4.1 2D simulations

We consider a small anisotropy coefficient of $\varepsilon(\theta) = 0.16(1 - 0.025\cos(4\theta))$. The crystal is grown under the driving force of a constant far-field heat flux. Because of the symmetry of initial data, the interfacial contours of only one-half of the interface are shown in the sequence of interface morphologies in Figs. 1 and 2. The pattern is clearly dendritic at later times. Because the surface tension is isotropic, this pattern develops solely under the influence of the anisotropic kinetics.

The details of how a side-branch is initiated and grows can be seen in Figs. 1 and 2. In Fig.1, the scaled tip velocity $\overline{V}$ of the x-primary arm in the scaled frame is shown as a function of $R(t)$; the true tip velocity V is shown as an inset. In the scaled frame, there are oscillations in tip velocity. Details of temperature distribution are shown in Fig. 2. It is seen that during the oscillation, the local maxima in $\overline{V}$ correlate well with the development of non-monotonic temperature distributions near the tip and the initiation of side-branches. Notice that these subtle oscillations are not observable in the true tip velocity as they are concealed by the overall growth dynamics. Thus, an accurate numerical method, capable of separating the dynamics of growth from those of shape change, is essential in exposing this oscillatory phenomena.

In Figs. 2[a]-[f], a sequence of interface morphologies and associated interface temperature distributions are shown, corresponding to the index marked along the $\overline{V}$ curve in Fig. 2. In the absence of externally imposed noise or disturbances, the interface develops negative curvature in synchrony with the interfacial temperature becoming non-monotone near the tip. The observed non-monotonicity of the temperature near the tip that stimulates the formation of dendritic side-branching is time periodic, which suggests the operation of a limit cycle rather than selective amplification of noise. The operation of the dendritic limit cycle involves progressive shape changes near the tip that eventually induce a non-monotonic temperature distribution. This leads to the development of a protuberance, changes in the sign of the interface curvature, and the formation of a side-branch as seen in Fig.2[a]-[f]. The cycle then repeats to produce another side-branch.

The shape, Fig. 2[a], has a monotonic temperature distribution as the tip is approached ($\alpha \to 0^{\pm}$). In Fig. 2[b] the circular shape becomes curved, and the interfacial temperature distribution changes correspondingly. In Fig. 2[c], a pair of local temperature maxima develop near $\alpha \approx 0.1$. The primary arm of the dendrite along the x-axis is about to form. In Fig. 2[d], a primary arm of the dendrite has already formed and negative curvature develops around $\alpha \approx 0.05$. The temperature distribution is about to become non-monotonic. In Fig. 2[e], although it is not apparent yet from the interface at the resolution shown, the interface curvature develops oscillations near the local temperature maxima (around $\alpha \approx 0.05$) that give rise to a small protuberance that will later grow into a side-branch. In Fig. 2[f], the small protuberance is now seen. The new local maxima in the temperature near $\alpha \approx 0.05$ become more apparent and the temperature around the tip (from $\alpha = 0$ to $\alpha \approx \pm 0.05$ becomes monotone again. As can be inferred from Fig. 2[g], new local maxima in the temperature occur and new protuberances will be produced. In Fig. 2[h], a small protuberance develops into a side-branch. This sequence

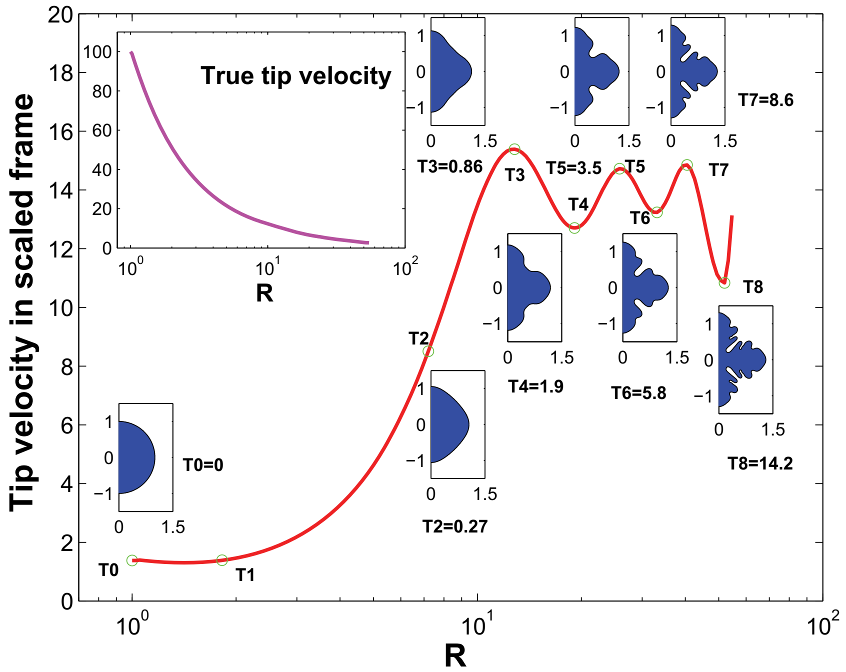

Figure 1: Boundary integral simulation of the evolution of a circular interface with anisotropic kinetics $\varepsilon(\theta) = 0.16(1-0.025cos(4\theta))$ and a constant far-field heat flux. The scaled velocity, $\overline{V}$, at the tip and the unscaled (true) tip velocity, V, are also shown. The evolution periodically generates side-branches when the temperature distribution near the tip becomes non-monotonic. These are reflected in the oscillations of $\overline{V}$. The tip grows faster than the surrounding interface, and subsequent negative curvatures are initiated at various locations along the interface where the temperature periodically becomes non-monotonic, suggestive of a dynamic limit cycle.

completes a limit cycle. The dynamical cycle is repeated indefinitely as suggested by the overall solidification pattern.

We next perform a refinement study to confirm that noise is not important here. Using the initial shape and $\varepsilon(\theta)$ described above, we perform two simulations: case one (with number of mesh points on the interface $N = 1,024$, time step $\Delta\bar{t} = 2.5E-4$, tolerance for convergence of GMRES $tol = 1.0E-6$) and case two (with $N = 4,096$, $\Delta\bar{t} = 1.0E-4$, $tol = 1.0E-12$). Note that tol is a crucial parameter in determining the accuracy of the computed normal velocity in GMRES. The smaller the tol, the more accurate the calculation of normal velocity. Fig.3 shows the comparison of the interface morphology at $\bar{t} = 0.39$. As can be seen from Fig.3, the dendritic shapes for these two cases agree very well. The lack of significant noise is due to the fact that this method is spectrally accurate and that the heat flux used is well below that for which noise from discretization and rounding errors could be significantly amplified during the computation. The detailed validition of the spectral accuracy of the numerical algorithm can be found in [Li, Lowengrub, and Leo (2007); Hou, Lowengrub, and Shelley (1994)].

4.2 3D simulations

In 3D, the results are qualitatively similar to those obtained in 2D when the flux $\overline{J} = C\overline{R}$, where C is a constant. The flux used here corresponds roughly to assuming a constant far-field temperature boundary condition. In Figs. 4 and 5, results are presented using an initially spherical crystal with anisotropic kinetic coefficient, $\varepsilon(\mathbf{n}) = \varepsilon_0(1-\beta(3-4[n_1^4+n_2^4+n_3^4]))$, $\varepsilon_0 = 0.1$ and anisotropy

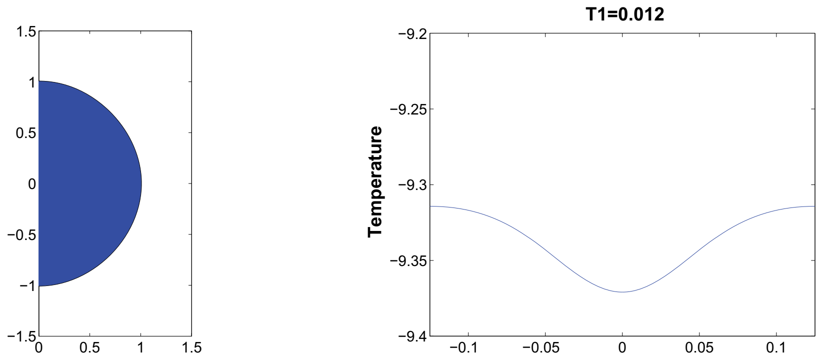
T1=0.012
Temperature
α
1.5
1
0.5
0
−0.5
−1
−1.5
−9.2
−9.25
−9.3
−9.35
−9.4
−0.1
−0.05
0.05
0.1

[a]

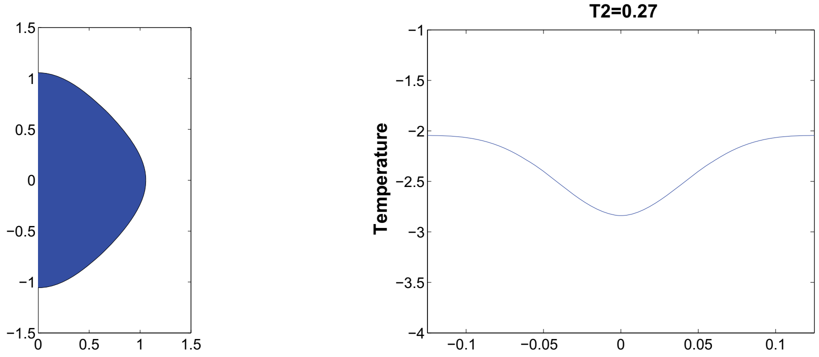
T2=0.27
Temperature
α
−1
−1.5
−2
−2.5
−3
−3.5
−4

[b]

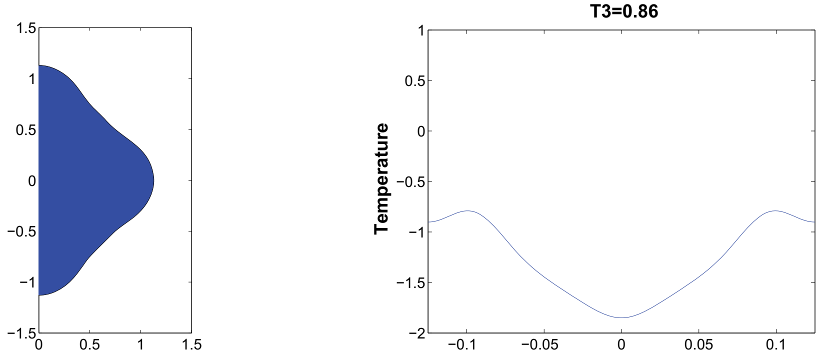
T3=0.86
Temperature
α
1
0.5
0
−0.5
−1
−1.5
−2

[c]

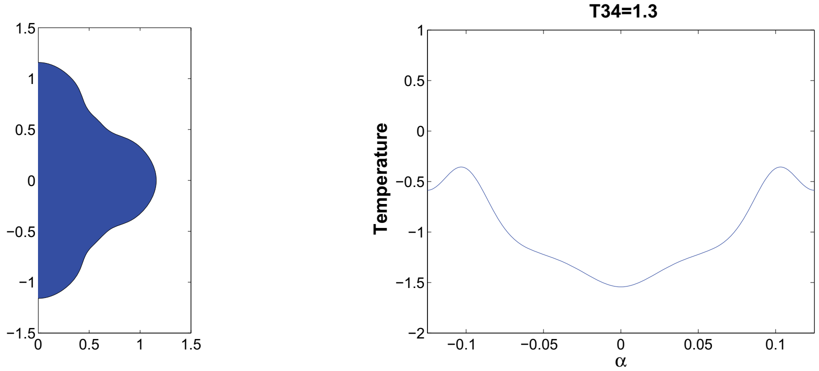
T34=1.3
Temperature
α
1
0.5
0
−0.5
−1
−1.5
−2

[d]

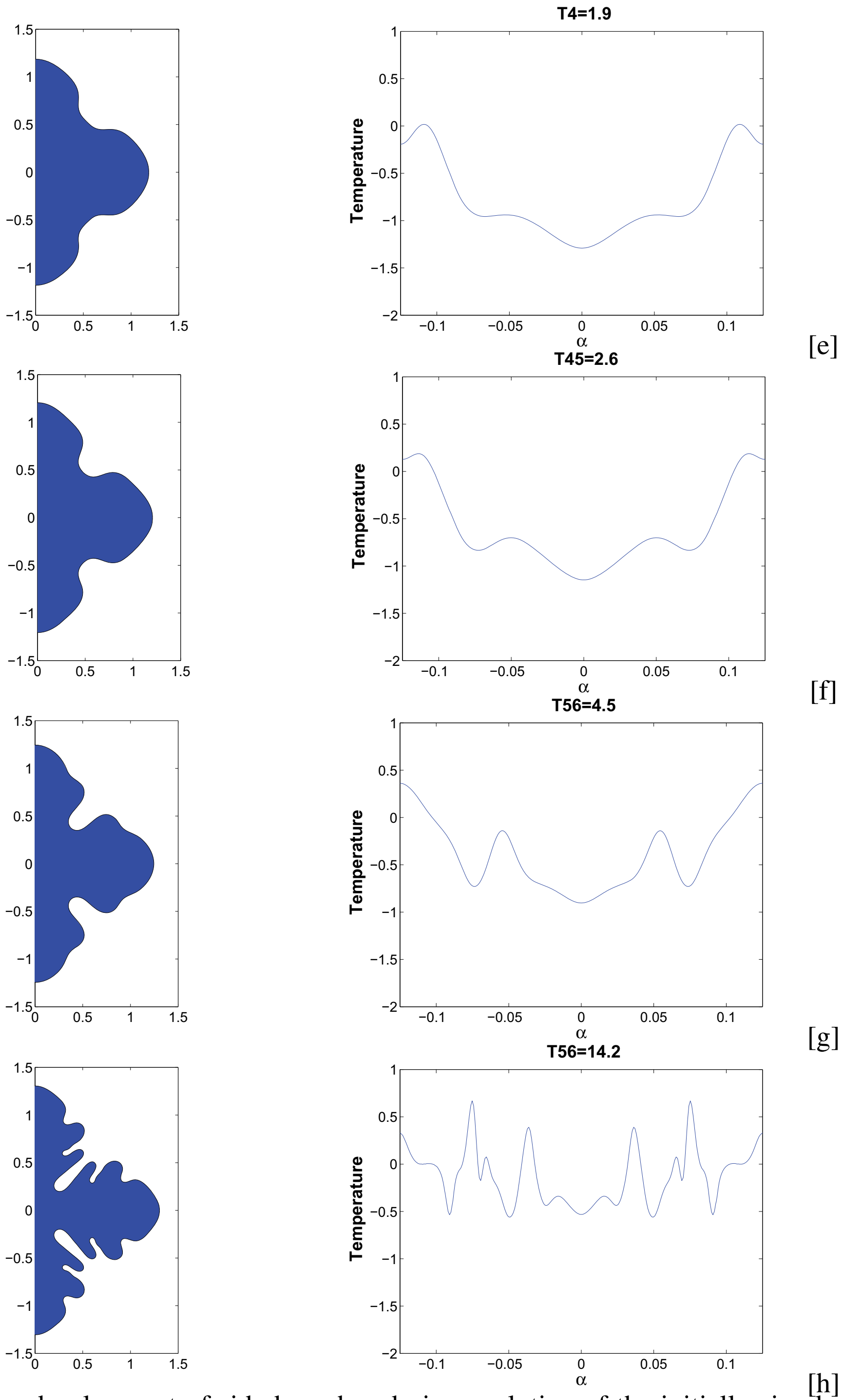

Figure 2: Details of the development of side-branches during evolution of the initially circular interface, suggestive of the operation of a limit cycle. [a] T1 = 0.012: Starting from a circle, with a monotone-down interface temperature as the tip, $\alpha \to 0^{\pm}$ is approached. [b] T2 = 0.27: Shape becomes non-circular and a primary arm starts to form. [c] T3 = 0.86: Maxima in the temperature develop near $\alpha = 0.1$. Dendrite tip forms. [d] T34 = 1.3: The temperature becomes non-monotone around $\alpha = 0.05$. [e] T4 = 1.9 and [f] T45 =2.6: Negative curvatures form ahead of the growing protuberances, and additional new temperature maxima develops near $\alpha = 0.05$. A pair of protuberance forms. [g] T=4.5: The protuberances develop into side-branches. The temperature near the tip becomes monotonic. [h] T=14.2: Well developed side-branches.

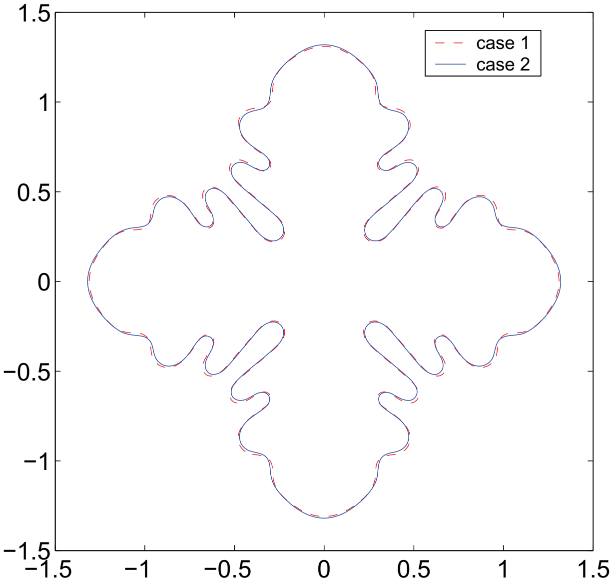

Figure 3: A comparison of coarse and fine resolution for interface morphology at $\bar{t} = 0.039$. The parameters used for case 1 (coarse) are: number of mesh points on interface $N = 1,024$, time step $\Delta\bar{t} = 2.5E-4$, tolerance for convergence of GMRES $tol = 1.0E-6$) ; The parameters used for case 2 (fine) are: $N = 4,096$, $\Delta\bar{t} = 1.0E-4$, $tol = 1.0E-12$, where tol is the tolerance used in GMRES to determine the accuracy of the normal velocity calculation. The kinetic coefficient is $\varepsilon(\theta) = 0.16(1-0.025cos(4\theta))$ and a constant far-field heat flux is $J = 100$.

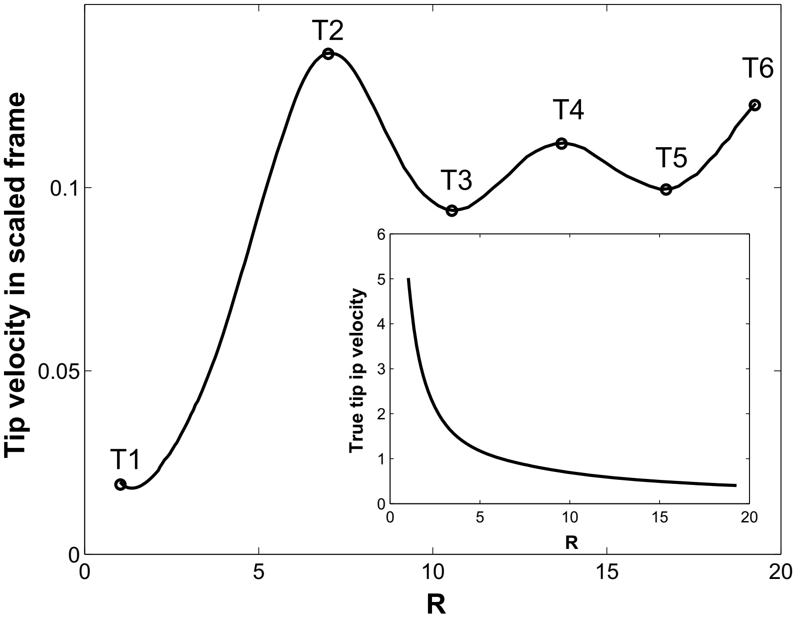

Figure 4: Three dimensional boundary integral simulation of the evolution of a spherical interface with a far-field heat flux increasing linearly in $R(t)$. The anisotropic kinetic coefficient, $\varepsilon(\mathbf{n}) = \varepsilon_0(1-\beta(3-4[n_1^4 + n_2^4 + n_3^4]))$, where $\mathbf{n}$ is the outwards normal of the interface with three components n_1, n_2 and n_3, $\varepsilon_0 = 0.1$ and anisotropy $\beta = 0.1$. The scaled velocity, $\overline{V}$, at the tip and the unscaled (true) tip velocity, V, are also shown. Similar to the two dimensional case, there are oscillations of $\overline{V}$, which suggest a dynamic limit cycle that gives rise to the formation of side-branches as shown in the following sequence of morphologies.

$\beta = 0.1$. In Fig. 4, the scaled velocity, $\overline{V}$, at the tip and the unscaled (true) tip velocity, V, are also shown. As in 2D, there are oscillations of $\overline{V}$, which suggest the presence of a limit cycle that gives rise to the formation of side-branches. In Fig. 5, the crystal morphologies are shown during the evolution (the last frame shows the adaptive mesh). As in 2D, the primary arms form followed by a succession of side-branches the origin of which corresponds to the oscillations observed in the normal velocity that arise through a non-monotonic temperature distribution near the tip (not shown).

5 Conclusion and discussion

In this paper, we investigated the existence of a deterministic mechanism for side-branching in dendritic growth under an anisotropic kinetic boundary condition. We developed accurate 2D and 3D boundary integral methods in which a time and space rescaling scheme is implemented in a manner such that the area/volume of the crystal appears unchanged. By scaling out the overall growth of the evolving crystal, we were able to track the detailed dynamics of dendrite tip. The numerical results reveal that the interface can develop a non-monotone temperature distribution that leads to the oscillations of the scaled tip velocity that behaves like a limit cycle and generates a sequence of protuberances near the tip that propagate away from the tip and form side-branches at later times. The formation of side-branches is intrinsic to the dynamics and occurs without noise, solely under the deterministic influence of the anisotropic kinetic boundary condition.

Similar phenomena were observed in our previous work [Glicksman, Lowengrub, and Li (2006)], in which the competing anisotropies of the shape and of the surface energy were investigated with regard to the development of side-branching. In [Glicksman, Lowengrub, and Li (2006)], a careful analysis of the Gibbs-Thomson-Herring (GTH) boundary condition shows that the combination of shape anisotropy, i.e., an elongated shape in one spatial direction, with surface energy anisotropy also leads to non-monotone equilibrium temperature distributions. As in the results presented here, a sequence of non-monotonicities in temperature occurs close to the tip, and the temperature field interacts dynamically with the evolving shape. It appears that each time local temperature maxima occur, curvature oscillations develop slightly aft of the tip. These curvature oscillations stimulate the formation of a pair of protuberances, which in most cases continue to grow and form opposing, coherent side-branches.

Though the circular shape used in this paper is not dendritic initially, the anisotropic interfacial kinetics drives the interface to evolve along its preferred direction, and the primary arms of the dendrite form accordingly. A detailed analysis of the coupling between temperature distribution and interface morphologies shows that the mechanisms for side-branching are similar to what we observed in [Glicksman, Lowengrub, and Li (2006)]. The pattern formation mechanism uncovered here and [Glicksman, Lowengrub, and Li (2006)] rely solely on the interface boundary condition. Other interesting morphological phenomena concerning the directional solidification of alloys, such as the cell-to-dendrite transition, and the relationship of side-branch spacings to the solidification parameters might also require reinterpretation based on the non-monotonic behavior of the interface boundary condition disclosed herein.

Careful experimental observations, such as accomplished in the Isothermal Dendritic Growth Experiment [LaCombe, Koss, Frei, Giummarra, Lupulescu, and Glicksman (2002); Giummarra, LaCombe, Koss, Frei, Lupulescu, and Glicksman (2005)], seldom reveal coherent side-branching, but this fact might simply be caused by the fact that the thermal fields during dendritic growth are never perfectly steady or symmetrical about the growth axis. Also, what seems especially significant about the simulations of dendritic pattern formation reported here is that perturbations to the crystal-melt interface, and selective amplification of noise, do not play a significant role in the process. The interface boundary condition itself seems to provide a deterministic dynamical condition that, when combined with sufficient shape and energy anisotropies, is fully capable of induc-

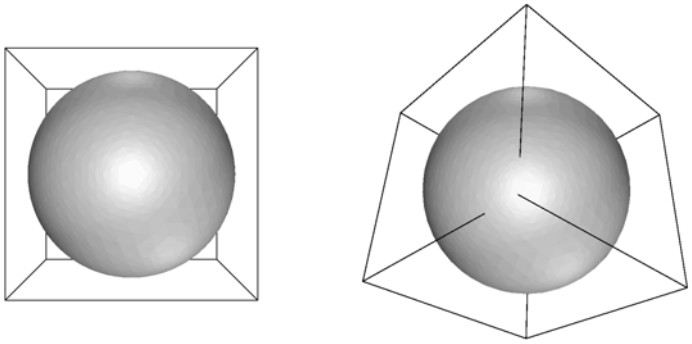

[T1, R=1.0]

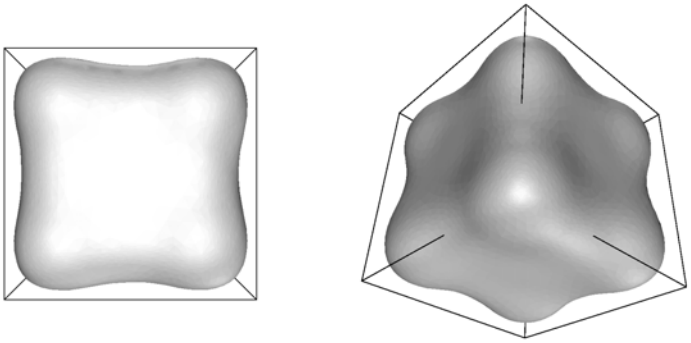

[T2, R=7.0]

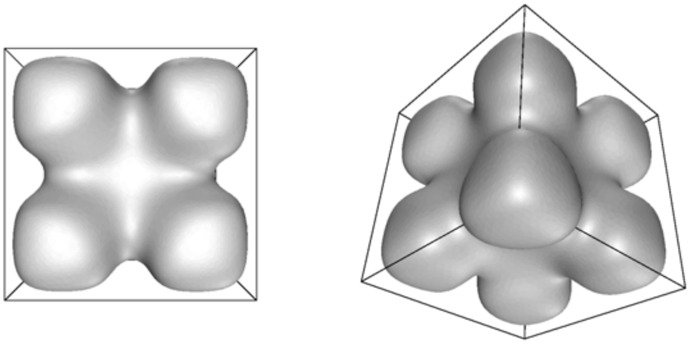

[T3, R=10.6]

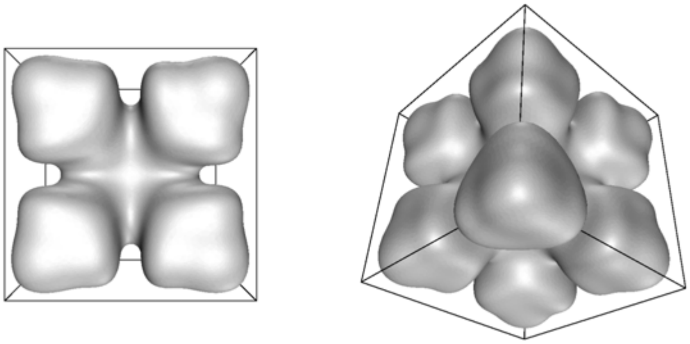

[T4, R=13.7]

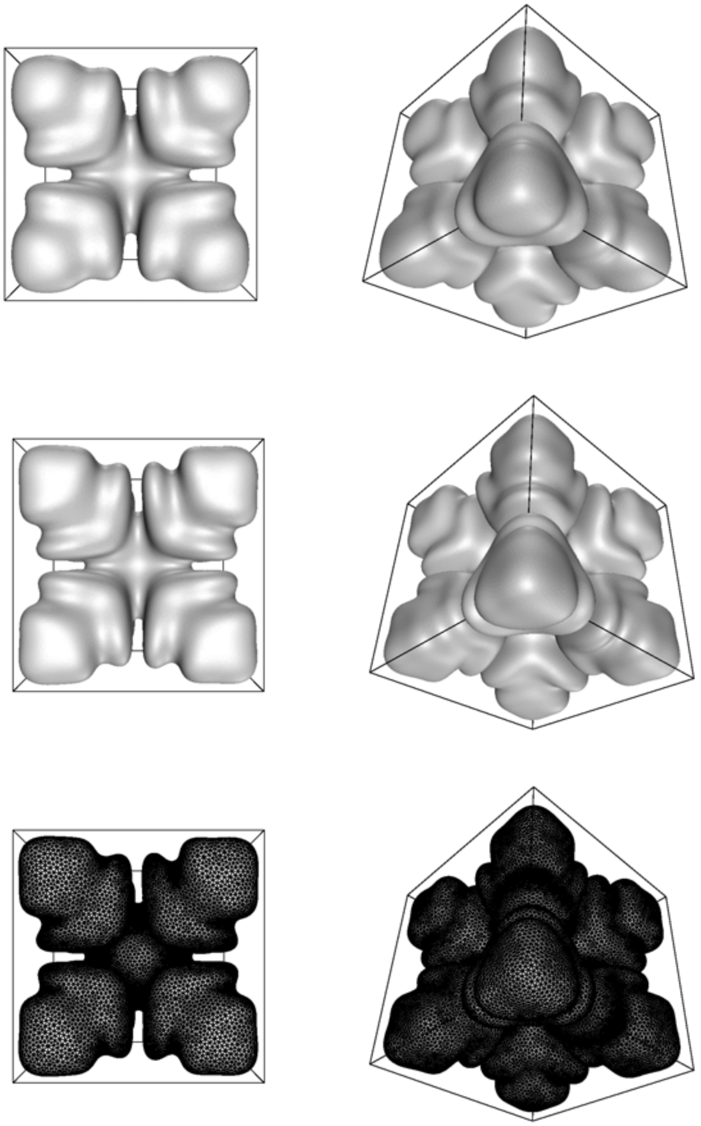

[T5, R=16.07]

[T6, R=19.3]

[T6, R=19.3]

Figure 5: Details of the development of side-branches during evolution of a sphere interface with a far-field heat flux increasing linearly in $R(t)$. The number of points $N = 362$ initially and $N = 29,280$ at the final image shown.

ing a limit cycle behavior near the tip. The origin of dendritic side-branching might be fundamentally different from current conventional concepts.

Acknowledgement: JSL, XL and SL acknowledge support from the National Science Foundation (DMS) and the generous computing resources from the Network and Academic Computing Services at University of California at Irvine (NACS) and computing resources of BME department (U.C. Irvine). MEG is grateful for support provided through the John Tod Horton Distinguished Professorship of Materials Science and Engineering at Rensselaer Polytechnic, and from the University of Florida. Thanks are also extended to the National Aeronautics and Astronautics Administration, NASA, Washington, DC, for their financial and operational support of the Isothermal Dendritic Growth Experiment (IDGE).

References

Almgren, R.; Dai, W.; Hakim, V. (1993): Scaling behavior in anisotropic Hele-Shaw flow. *Phys. Rev. Lett.*, vol. 71, pp. 3461–3464.

Borzsonyi, T.; Toth-Katona, T.; Buka, A.; Granasy, L. (2000): Regular dendritic patterns induced by nonlocal time-periodic forcing. *Phys. Rev. E*, vol. 62, pp. 7817–7827.

Couder, Y.; Cardoso, O.; Dupuy, D.; Tavernier, P.; Thom, W. (1986): Dendritic growth in the Saffman-Taylor experiment. *Euro. Phys. Lett.*, vol. 2, pp. 437–443.

Couder, Y.; Gerard, N.; Rabaud, M. (1986): Narrow fingers in the Saffman-Taylor instability. *Phys. Rev. A*, vol. 34, pp. 5175–5178.

Cristini, V.; Blawzdziewicz, J.; Loewenberg, M. (2001): An adaptive mesh algorithm for evolving surfaces: Simulations of drop breakup and coalescence. *J. Comp. Phys.*, vol. 168, pp. 445–463.

Cristini, V.; Lowengrub, J. (2004): Three-dimensional crystal growth- II. Nonlinear simulation and control of the Mullins-Sekerka instability. *J. Crystal Growth*, vol. 266, pp. 552–567.

Dougherty, A.; Kaplan, P.; Gollub, J. (1987): Development of side branching in dendritic crystal growth. *Phys. Rev. Lett.*, vol. 58, pp. 1652–1655.

Fast, P.; Kondic, L.; Palffy-Muhoray, P.; Shelley, M. (2001): Pattern formation in non-Newtonian Hele Shaw flow . *Phys. fluid*, vol. 13, pp. 1191–1212.

Gibou, F.; Min, C.; Ceniceros, H. (2007): Non-Graded Adaptive Grid Approaches to the Incompressible Navier-Stokes Equations. *FDMP: Fluid Dynamics and Materials Processing*, vol. 3, pp. 37–48.

Giummarra, C.; LaCombe, J.; Koss, M.; Frei, J.; Lupulescu, A.; Glicksman, M. (2005): Sidebranch characteristics of pivalic acid dendrites grown under convection-free and diffuso-convective conditions. *J. Crystal Growth*, vol. 274, pp. 317–330.

Glicksman, M.; Lowengrub, J.; Li, S. (2006): Non-monotone temperature boundary conditions in dendritic growth. *Proc. in Modelling of Casting, Welding and Adv. Solid. Processes XI.*, pp. 521–528. Eds. C. A. Gandin and M. Bellet.

Glicksman, M.; Schaefer, R.; Ayers, J. (1976): Dendritic growth–test of theory. *Metall. Trans. A*, vol. 7, pp. 1747.

Herring, C. (1951): *Physics of powder metallurgy*. McGraw-Hill, New York. Eds. W.E. Kingston.

Hong, C.; Zhu, M.; Lee, S. (2006): Modeling of Dendritic Growth in Alloy Solidification with Melt Convection. *FDMP: Fluid Dynamics and Materials Processing*, vol. 2, pp. 247–260.

Hou, T.; Lowengrub, J.; Shelley, M. (1994): Removing the stiffness from interfacial flows with surface tension. *J. Comp. Phys.*, vol. 114, pp. 312–338.

Ihle, T. (2000): Competition between kinetic and surface tension anisotropy in dendritic growth. *The Euro. Phys. Journal B*, vol. 16, pp. 337–344.

Jacob, E.; Garik, P. (1990): The formation of patterns in non-equilibrium growth. *Nature*, vol. 343, pp. 523–530.

Jeong, J.; Goldenfeld, N.; Dantzig, J. (2001): Phase field model for three-dimensional dendritic growth with fluid flow. *Phys. Rev. E*, vol. 64, pp. 041602–1–041602–14.

Jou, H.; Leo, P.; Lowengrub, J. (1997): Microstructural evolution in inhomogeneous elastic media. *J. Comp. Phys.*, vol. 131, pp. 109–148.

Karma, A.; Rappel, W. (1999): Phase-field model of dendritic sidebranching with thermal noise. *Phys. Rev. E*, vol. 60, pp. 3614–3625.

Kim, Y.; Goldenfeld, N.; Dantzig, J. (2000): Computation of dendritic microstructures using a level set method. *Phys. Rev. E*, vol. 62, pp. 2471–2474.

Kondic, L.; Palffy-Muhoray, P.; Shelley, M. (1996): On models of Non-Newtonian Hele-Shaw flow. *Phys. Rev. E*, vol. 54, pp. 4536–4539.

Kondic, L.; Palffy-Muhoray, P.; Shelley, M. (1997): Non-Newtonian Hele-Shaw flow and the Saffman-Taylor instability. *Phys. Rev. Lett.*, vol. 80, pp. 1433–1436.

LaCombe, J.; Koss, M.; Frei, J.; Giummarra, C.; Lupulescu, A.; Glicksman, M. (2002): Evidence for tip velocity oscillations in dendritic solidification. *Phys. Rev. E*, vol. 65, pp. 031604–1–031604–6.

Li, S.; Lowengrub, J.; Leo, P. (2005): Nonlinear morphological control of growing crystals. *Physica D*, vol. 208, pp. 209–219.

Li, S.; Lowengrub, J.; Leo, P. (2007): A rescaling scheme with application to the long time simulation of viscous fingering in a Hele-Shaw cell. *J. Comp. Phys.*, vol. in press.

Li, S.; Lowengrub, J.; Leo, P.; Cristini, V. (2004): Nonlinear theory of self-similar crystal growth and melting. *J. Crystal Growth*, vol. 267, pp. 703–713.

Li, S.; Lowengrub, J.; Leo, P.; Cristini, V. (2005): Nonlinear stability analysis of self-similar crystal growth: control of the MullinsSekerka instability. *J. Crystal Growth*, vol. 277, pp. 578–592.

Li, X.; Cristini, V.; Nie, Q.; Lowengrub, J. (2007): Nonlinear three-dimensional simulation of solid tumor growth. *Discrete Dyn. Sys. B*, vol. 7, pp. 581–604.

Martin, O.; Goldenfeld, N. (1987): Origin of sidebranching in dendritic growth. *Phys. Rev. A*, vol. 35, pp. 1382–1390.

McFadden, G.; Coriell, S.; Sekerka, R. (2000): Effect of surface free energy anisotropy on dendrite tip shape. *Acta Materialia*, vol. 48, pp. 3177–3181.

McFadden, G.; Coriell, S.; Sekerka, R. (2000): Analytic solution for a non-axisymmetric isothermal dendrite. *J. Crystal Growth*, vol. 208, pp. 726–745.

Mikhlin, S. (1957): *Integral equations and their applications to certain problems in mechanics, mathematical physics and Technology*. Pergamon.

Narski, J.; Picasso, M. (2007): Adaptive 3D finite elements with high aspect ratio for dendritic growth of a binary alloy including fluid flow induced by shrinkage. *FDMP: Fluid Dynamics and Materials Processing*, vol. 3, pp. 49–64.

Nash, G.; Glicksman, M. (1974): Capillarity-limited steady-state dendritic growth–I. theoretical development. *Acta Metall.*, vol. 22, pp. 1283.

Nash, G.; Glicksman, M. (1974): Capillarity-limited steady-state dendritic growth–II. numerical results. *Acta Metall.*, vol. 22, pp. 1291.

Pieters, R.; Langer, J. (1986): Noise-driven sidebranching in the Boundary-Layer model of dendritic solidification. *Phys. Rev. Lett.*, vol. 56, pp. 1948–1951.

Saad, Y.; Schultz, M. (1986): GMRES: a generalized minimal residual algorithm for solving nonsymmetric linear systems. *SIAM J. Sci. Stat. Comput.*, vol. 7, pp. 856–869.

Sussman, M.; Ohta, M. (2007): Improvements for calculating two-phase bubble and drop motion using an adaptive sharp interface method. *FDMP: Fluid Dynamics and Materials Processing*, vol. 3, pp. 21–36.

Zinchenko, A.; Rother, M.; Davis, R. (1997): A novel boundary integral algorithm for viscous interaction of deformable drops. *Phys. Fluids*, vol. 9, pp. 1493–1511.